

**Cosmological redshift-space distortion
on clustering of high-redshift objects:
correction for nonlinear effects in power spectrum
and tests with N-body simulations**

Hiromitsu Magira, Y. P. Jing¹ and Yasushi Suto¹

Department of Physics, School of Science, University of Tokyo, Tokyo 113-0033, Japan.

ABSTRACT

We examine the cosmological redshift-space distortion effect on the power spectrum of the objects at high-redshifts, which is an unavoidable observational contamination in general relativistic cosmology. In particular, we consider the nonlinear effects of density and velocity evolution using high-resolution N-body simulations in cold dark matter models. We find that the theoretical modeling on the basis of the fitting formulae of nonlinear density and velocity fields accurately describes the numerical results, especially in quasi-nonlinear regimes. These corrections for nonlinear effects are essential in order to use the the cosmological redshift-space distortion as a cosmological test. We perform a feasibility test to derive constraints from the future catalogues of high-redshift quasars using our theoretical modeling and results of N-body simulations. Applying the present methodology to the future data from on-going surveys of high-redshift galaxies and quasars will provide a useful tool to constrain a geometry of the universe.

Subject headings: cosmology: theory - distance scale - dark matter - large-scale structure of the universe – galaxies: distances and redshifts – quasars: general – methods: numerical

1. Introduction

The observational cosmology is now entering a new and exciting phase where the high-redshift universe can be directly and systematically mapped by observation. Lyman-break galaxies at $z \approx 3$ (Steidel et al. 1996, 1998) already placed a strong constraint on the nature and evolution of the hosting haloes at the high redshifts (Jing & Suto 1998). The Sloan Digital Sky Survey (SDSS)

¹also at Research Center for the Early Universe, School of Science, University of Tokyo, Tokyo 113-0033, Japan.

will complete a homogeneous catalogue of $\sim 10^5$ QSOs even extending $z \gtrsim 5$; in fact, the highest- z QSO as of this writing (SDSSp J033829.31+002156.3 at $z = 5.00$) was discovered from the SDSS commissioning data (Fan et al. 1999). Haiman & Loeb (1999) predict that the *Chandra X-ray Observatory* will detect ~ 100 QSOs at $z \gtrsim 5$ per its $17' \times 17'$ field of view.

Those datasets will necessarily and significantly change the way of research of the clustering of objects at high redshifts. Due to the statistical limitation of existing catalogues of QSOs, it has been common to infer its clustering amplitude and evolution in a model-dependent and indirect manner (but see, e.g., La Franca, Andreani, & Cristiani 1998); an interesting example of this methodology is the use of the fluctuation in the X-ray background (e.g., Lahav, Piran, & Treyer 1997; Treyer et al. 1998). In near future, however, one can analyze the QSOs redshift catalogues in order to detect the clustering at $z \sim 5$ as is routinely repeated for the existing galaxy redshift samples at $z \lesssim 0.1$.

In extracting the cosmological information from such catalogues of objects at high redshifts, there are several observational “contaminations” that one has to keep in mind, including

linear redshift-space (velocity) distortion: in linear theory of gravitational evolution of fluctuations, any density fluctuations induce the corresponding peculiar velocity field, which results in the systematic distortion of the pattern of distribution of objects in redshift space. The analytical expression for the linear distortion was first given by Kaiser (1987) and then later elaborated by a number of people (see Hamilton 1998 for an excellent review).

nonlinear redshift-space (velocity) distortion: virialized nonlinear objects have an isotropic and large velocity dispersion. This *finger-of-God* effect significantly suppresses the observed amplitude of correlation on small scales (Davis & Peebles 1983; Suto & Sugimoto 1991). An empirical expression for this effect in the power spectrum was discussed by Peacock & Dodds (1994, 1996; PD) and Cole, Fisher, & Weinberg (1994, 1995).

cosmological redshift-space (geometry) distortion: while the geometry of the local universe is well approximated as Euclidean, the global structure of the universe should be properly described by a general relativistic model. In particular, the comoving separation of a pair of objects at $z \gg 0.1$ is not determined only by their observable angular and redshift separations ($\delta\theta$, and δz) without specifying the geometry, or equivalently the matter content, of the universe (i.e., the cosmological density parameter Ω_0 , and the dimensionless cosmological constant λ_0). This generates a nontrivial anisotropy in the clustering pattern of objects, particularly at $z \gtrsim 1$ (Alcock & Paczyński 1979; Matsubara & Suto 1996; Ballinger, Peacock, & Heavens 1996; Popowski et al. 1998).

cosmological light-cone effect: all cosmological observations are carried out on a light-cone, the null hypersurface of an observer at $z = 0$, and not on any constant-time hypersurface. Thus clustering amplitude and shape of objects should naturally evolve even *within* the survey volume of a given observational catalogue. Unless restricting the objects at a narrow bin of z at the expense of the statistical significance, the proper understanding of the data requires a

theoretical model to take account of the average over the light cone which has been extensively discussed by our group (Nakamura, Matsubara, & Suto 1998; Matsubara, Suto, & Szapudi 1997; Yamamoto & Suto 1999; Nishioka & Yamamoto 1999; Suto et al. 1999; Yamamoto, Nishioka, & Suto 1999) and others (e.g., Mataresse et al. 1997; Moscardini et al. 1998; de Laix & Starkman 1998).

bias: the final difficulty in relating the clustering of any species of astronomical objects to that of mass fluctuations is the biasing (Kaiser 1984). While the first three are purely dynamical (or gravitational) effects, the biasing of luminous objects relative to mass should result from a complicated and delicate competition of a variety of astrophysical processes, which is almost impossible to describe from the first principle. Therefore a parametric description of the biasing on the basis of simple assumptions is useful at this point in understanding the generic features of the possible effects (e.g., Bardeen et al. 1985; Mo & White 1996; Fry 1996; Jing 1998; Taruya, Koyama, & Soda 1999; Suto et al. 1999b).

The first two effects are already important in any shallow surveys of objects at $z \sim 0$ (see e.g., Hatton & Cole 1998), and the last three effects become progressively important as the survey becomes deeper.

While one of the primary scientific goals for the cosmological surveys is a proper understanding of the clustering evolution of luminous objects at high redshifts, one can probe the geometry of the universe combining the standard theory of structure formation. This is what we will explore in the present paper. Our previous work (Suto et al. 1999a) examined the two-point correlation function in cosmological redshift space, and found that the nonlinear peculiar velocity field, or *finger-of-God*, cannot be neglected even on fairly large scales. Thus here we focus on the power spectrum, which is easier to describe the nonlinear effects theoretically (PD; Ballinger et al. 1996). We focus on the mass power spectrum and do not consider the biasing explicitly below, while the same methodology is applicable if the bias is linear and scale-independent. In reality, however, the bias, especially for galaxies and quasars, may be too complicated to be analytically tractable (i.e., Dekel & Lahav 1999; Taruya, Koyama, & Soda 1999). This issue will be studied in detail and described elsewhere (Magira, Jing, Taruya, & Suto 1999).

The rest of the paper is organized as follows. First we describe a theoretical modeling of the power spectrum of *dark matter* including the cosmological redshift-space distortion in addition to the linear and nonlinear velocity distortions (§2). The theoretical model prediction is checked and calibrated against the N-body simulations. Next we examine the feasibility of estimating cosmological parameters by analyzing the anisotropy in the monopole and quadrupole moments of power spectra of objects at high redshifts with the SDSS QSO sample specifically in mind (§3). Finally §4 is devoted to discussion and conclusions.

2. Modeling nonlinear redshift-space distortion on power spectrum

2.1. Distortion due to the peculiar velocity

The power spectrum distorted by the peculiar velocity field (neglecting the cosmological distortion for the moment), $P^{(S)}(k; z)$, is known to be well approximated by the following expression (Peacock & Dodds 1994; Cole et al. 1995):

$$P^{(S)}(k_{\perp}, k_{\parallel}; z) = P^{(R)}(k; z) \left[1 + \beta(z) \left(\frac{k_{\parallel}}{k} \right)^2 \right]^2 D[k_{\parallel} \sigma_P(z)], \quad (1)$$

where k_{\perp} and k_{\parallel} are the comoving wavenumber perpendicular and parallel to the line-of-sight of an observer, and $P^{(R)}(k; z)$ is the power spectrum in real space. The second factor in the right-hand-side of equation (1) represents the linear redshift-space distortion derived by Kaiser (1987) adopting the distant-observer approximation and the scale-independent linear bias, $b(z)$. Then $\beta(z)$ is defined by

$$\beta(z) \equiv \frac{1}{b(z)} \frac{d \ln D(z)}{d \ln a} \simeq \frac{1}{b(z)} \left[\Omega^{0.6}(z) + \frac{\lambda(z)}{70} \left(1 + \frac{\Omega(z)}{2} \right) \right], \quad (2)$$

$$\Omega(z) = \left[\frac{H_0}{H(z)} \right]^2 (1+z)^3 \Omega_0, \quad (3)$$

$$\lambda(z) = \left[\frac{H_0}{H(z)} \right]^2 \lambda_0, \quad (4)$$

where $H(z)$ is the Hubble parameter at redshift z :

$$H(z) = H_0 \sqrt{\Omega_0(1+z)^3 + (1 - \Omega_0 - \lambda_0)(1+z)^2 + \lambda_0}. \quad (5)$$

The finger-of-God effect is modeled by the damping function $D[k_{\parallel} \sigma_P]$, which is the Fourier transform of the distribution function $f_v(v_{12})$ of pairwise peculiar velocities in real space. It has been often assumed that $f_v(v_{12})$ is exponential with a scale-independent pairwise velocity dispersion, σ_P . While this exponential function has been adopted in the literature (Cole et al. 1994, 1995; PD; Ballinger et al. 1996), its *predictability* was not fully checked against the N-body simulations; the previous studies used the value of σ_P determined *a priori* from the simulation data themselves. In reality, however, the formula is useful for the present purpose only if $\sigma_P(z)$ can be computed from a given $P^{(R)}(k; z)$ and a set of cosmological parameters (Ω_0 , λ_0 , σ_8 and H_0). In next subsections, we will show that $P^{(S)}(k_{\perp}, k_{\parallel}; z)$ combined with the existing fitting formulae for nonlinear density and velocity fields is in excellent agreement with the results of our high-resolution N-body simulations.

2.2. Pairwise velocity distribution function from N-body simulations

In order to quantify various effects of redshift-space distortion and to examine the validity of theoretical predictions, we use a series of high-resolution N-body simulations by Jing & Suto

(1998). The simulations assume representative cosmological models in cold dark matter (CDM) cosmogonies (Table 1). Each model has three different realizations, and employs $N = 256^3$ dark matter particles in the periodic comoving cube of the boxsize $L_{\text{box}} = 300h^{-1}\text{Mpc}$. We use the transfer function of Bardeen et al. (1985; BBKS) characterized by the shape parameter Γ , and the fluctuation amplitude is normalized by using σ_8 from the cluster abundance (Kitayama & Suto 1997). In the conventional CDM models, the shape parameter Γ is written in terms of Ω_0 , h and Ω_b , the baryon density parameter:

$$\Gamma = \Omega_0 h \exp(-\Omega_b - \sqrt{2h}\Omega_b/\Omega_0), \quad (6)$$

(Sugiyama 1995). In order to separate the resulting effect due to the shape of density fluctuations from those due to the geometry and evolution of the universe, we consider cases where Γ is treated as an independent parameter or given by equation (6) in §3. In the latter case, we assume that each simulation adopts $h \equiv \Gamma/\Omega_0$ neglecting Ω_b for definiteness.

First we compute the distribution function $f_v(v_{12})$ of pairwise velocity v_{12} from the entire simulation particles in order to determine the functional form of the damping function $D[k_{\parallel}\sigma_P]$. Figure 1 plots the pairwise peculiar velocity distribution function at $z = 0$ and $z = 2.2$ in three different models. Different symbols correspond to the results for different comoving separations. As simple analytical models for $f_v(v_{12})$, we consider an exponential:

$$f_v(v_{12}) = \frac{1}{\sqrt{2}\sigma_P} \exp\left(-\frac{\sqrt{2}|v_{12}|}{\sigma_P}\right), \quad (7)$$

and a Gaussian:

$$f_v(v_{12}) = \frac{1}{\sqrt{2}\sigma_P} \exp\left(-\frac{v_{12}^2}{2\sigma_P^2}\right). \quad (8)$$

The former is suggested to be a good approximation on nonlinear scales both observationally (Davis & Peebles 1983) and theoretically (Efstathiou et al. 1988; Ueda, Itoh, & Suto 1993; Suto 1993; Seto & Yokoyama 1998; Juszkiewicz et al. 1998), and the latter should be the case if the underlying density field is purely random-Gaussian.

Solid lines in Figure 1 represent the best-fit exponential distribution for results at $r = 45.5h^{-1}\text{Mpc}$, treating σ_P as a free parameter. The corresponding best-fit values are listed in Table 2.

Figure 1 indicates that neither exponential nor Gaussian function fits the numerical results completely. Thus it is reasonable that the best-fit values in Table 2 are somewhat different from the pairwise dispersions, $\sigma_{P,\text{sim}}$, directly evaluated from the N-body data. Dashed and dotted lines represent the exponential and Gaussian curves, respectively, both of which adopt $\sigma_{P,\text{sim}}$ as the velocity dispersion σ_P .

With this result in mind, however, we would still like to adopt the above distribution functions mainly for simplicity and definiteness. In fact we will show that this procedure is accurate enough for our present purpose. Thus the remaining task is to predict σ_P given a set of cosmological model

parameters. In a previous paper (Suto et al. 1999a), we find that a fitting formula by Mo, Jing, & Börner (1997; MJB hereafter) is in excellent agreement with our numerical results. Figure 2 plots $\sigma_{\text{P,sim}}$ as a function of the pair separation r for three models at $z = 0$ and 2.2. It is clear that $\sigma_{\text{P,sim}}$ asymptotically approaches the MJB formula:

$$\sigma_{\text{P,MJB}}^2 \equiv \Omega(z)H_0^2 \left[1 - \frac{1+z}{D^2(z)} \int_{\frac{1}{1+z}}^{\infty} \frac{D^2(z')}{(1+z')^2} dz' \right] \int_0^{\infty} \frac{dk}{k} \frac{\Delta_{\text{NL}}^2(k, z)}{k^2}. \quad (9)$$

Note that the original expression in MJB corresponds to the proper velocity, and the above equation (9) is converted in the comoving redshift space by multiplying a factor $[(1+z)c_{\perp}(z)]^2 = [(1+z)H_0/H(z)]^2$; see §2.3 and Suto et al. (1999a).

In order to examine whether the above prescription for the theoretical predictions is really consistent with the numerical simulations, we compute the multipole of the power spectrum in redshift space:

$$P_l^{(\text{S})}(k; z) \equiv \frac{2l+1}{2} \int_{-1}^1 d\mu P^{(\text{S})}(k, \mu; z) L_l(\mu), \quad (10)$$

where $\mu \equiv k_{\parallel}/k$ is the direction cosine, and L_l is the Legendre polynomials. Figure 3 shows the comparison of theoretical predictions and our numerical simulations of the angle averaged power spectrum, $P_0^{(\text{S})}(k; z)$ at $z = 0$ and 2.2.

Our theoretical predictions are based on the combination of the PD formula for $\Delta_{\text{NL}}^2(k, z)$ in real space and the MJB formula for σ_{P} . For definiteness we adopt an exponential distribution function (7) for the pairwise velocity, and the corresponding damping function in k -space is a Lorentzian:

$$D[k\mu\sigma_{\text{P}}] = \frac{1}{1 + (k\mu\sigma_{\text{P}})^2/2}. \quad (11)$$

Then equations (1) with equation (11) are analytically integrated; specifically the monopole and quadrupole moments are expressed as

$$P_0^{(\text{S})}(k, z) = \left[A(\kappa) + \frac{2}{3}\beta(z)B(\kappa) + \frac{1}{5}\beta^2(z)C(\kappa) \right] P^{(\text{R})}(k, z), \quad (12)$$

$$P_2^{(\text{S})}(k, z) = \left[\frac{5}{2} \{B(\kappa) - A(\kappa)\} + \beta(z) \left\{ \frac{4}{3}B(\kappa) + 3(C(\kappa) - B(\kappa)) \right\} \right. \\ \left. + \beta^2(z) \left\{ \frac{3}{2\kappa^2}(1 - C(\kappa)) - \frac{1}{2}C(\kappa) \right\} \right] P^{(\text{R})}(k, z), \quad (13)$$

$$A(\kappa) = \frac{1}{\kappa} \arctan(\kappa), \quad (14)$$

$$B(\kappa) = \frac{3}{\kappa^2} \left(1 - A(\kappa) \right), \quad (15)$$

$$C(\kappa) = \frac{5}{3\kappa^2} \left(1 - B(\kappa) \right), \quad (16)$$

with $\kappa(z) = k\sigma_{\text{P}}(z)/\sqrt{2}H_0$.

Incidentally, Cole et al. (1995) derived analogous expressions for the exponential distribution function of *one-dimensional* (i.e., not pairwise) velocity. This corresponds to a damping function:

$$\tilde{D}[k\mu\sigma_v] = \frac{1}{[1 + (k\mu\sigma_v)^2/2]^2}, \quad (17)$$

with σ_v being the one-dimensional velocity dispersion. Then they obtained

$$P_0^{(S)}(k, z) = \left[\tilde{A}(\tilde{\kappa}) + \frac{2}{3}\beta(z)\tilde{B}(\tilde{\kappa}) + \frac{1}{5}\beta^2(z)\tilde{C}(\tilde{\kappa}) \right] P^{(R)}(k, z), \quad (18)$$

$$P_2^{(S)}(k, z) = \left[\frac{5}{2} \left\{ \tilde{B}(\tilde{\kappa}) - \tilde{A}(\tilde{\kappa}) \right\} + \beta(z) \left\{ \frac{4}{3}\tilde{B}(\tilde{\kappa}) + 3(\tilde{C}(\tilde{\kappa}) - \tilde{B}(\tilde{\kappa})) \right\} + \beta^2(z) \left\{ \frac{5}{\tilde{\kappa}^2}(\tilde{B}(\tilde{\kappa}) - \tilde{C}(\tilde{\kappa})) \right\} \right] P^{(R)}(k, z), \quad (19)$$

$$\tilde{A}(\tilde{\kappa}) = \frac{\arctan(\tilde{\kappa}/\sqrt{2})}{\sqrt{2}\tilde{\kappa}} + \frac{1}{2 + \tilde{\kappa}^2}, \quad (20)$$

$$\tilde{B}(\tilde{\kappa}) = \frac{6}{\tilde{\kappa}^2} \left(A(\tilde{\kappa}) - \frac{2}{2 + \tilde{\kappa}^2} \right), \quad (21)$$

$$\tilde{C}(\tilde{\kappa}) = \frac{-10}{\tilde{\kappa}^2} \left(B(\tilde{\kappa}) - \frac{2}{2 + \tilde{\kappa}^2} \right), \quad (22)$$

with $\tilde{\kappa}(z) = k\sigma_v(z)/H_0$. If the velocity correlation is neglected, then σ_v is equal to $\sigma_P/\sqrt{2}$, and the above expressions agree with our results up to $O(\tilde{\kappa}^2)$ for $\tilde{\kappa} \ll 1$. While we use our expression in what follows, the result is insensitive to the choice because we mainly use the range $\tilde{\kappa} \ll 1$ for the statistical analysis.

As Figure 3 indicates, our theoretical predictions in redshift space (solid lines) are in good agreement with the simulation results (filled circles) especially for $k \lesssim 1h\text{Mpc}^{-1}$. For larger k , they start to deviate each other; while this might be ascribed to the approximation to the velocity distribution function, the similar discrepancy is recognized even in real space (dotted lines and open circles). As a matter of fact, we found that this is mainly ascribed to the smoothing effect resulting from the cloud-in-cell interpolation in computing the Fourier transform; we used 512^3 grids in estimating the power spectrum of simulation data. When we apply the correction for the smoothing effect in real space using the method described in Jing (1992), the results (crosses) agree better with the PD formula. Thus the discrepancy in the strongly nonlinear regime in Figure 3 is not real. In any case this does not affect our conclusions in this paper because we mainly use the range of $k \lesssim 0.2h\text{Mpc}^{-1}$ for the later analysis.

2.3. Theoretical predictions of the power spectrum in cosmological redshift space

In previous subsections, we have shown using our high-resolution N-body simulations that the power spectrum distorted by the peculiar velocity field (without the cosmological distortion) can be predicted fairly accurately by a combination of the existing fitting formulae. The expression for

the power spectrum in cosmological redshift space has been derived by Ballinger et al. (1996). In this subsection, we simply summarize their result using our own notation adopted in the paper for definiteness. Then we examine the extent to which the overall predictions are consistent with the N-body results in later subsections.

Consider a pair of objects located at redshifts z_1 and z_2 whose redshift difference $\delta z \equiv z_1 - z_2$ is much less than the mean redshift $z \equiv (z_1 + z_2)/2$. Then the *observable* separations of the pair perpendicular and parallel to the line-of-sight direction, $x_{s\perp}$ and $x_{s\parallel}$, are given as $z\delta\theta/H_0$ and $\delta z/H_0$, respectively ($\delta\theta$ is the angular separation of the pair on the sky). Then the mapping of the comoving separation in real space (x_\perp, x_\parallel) to that in CRD (cosmological redshift distortion) space is expressed as

$$x_{s\perp}(z) = x_\perp/c_\perp(z), \quad x_{s\parallel}(z) = x_\parallel/c_\parallel(z), \quad (23)$$

where $c_\parallel(z) = H_0/H(z)$, $c_\perp(z) = H_0(1+z)d_A(z)/z$, and $d_A(z)$ is the angular diameter distance (Matsubara & Suto 1996; Ballinger et al. 1996; Suto et al. 1999a).

Then the power spectrum in the CRD space is

$$P^{(\text{CRD})}(k_{s\perp}, k_{s\parallel}; z) = \frac{1}{c_\perp(z)^2 c_\parallel(z)} P^{(\text{S})} \left(\frac{k_{s\perp}}{c_\perp(z)}, \frac{k_{s\parallel}}{c_\parallel(z)}; z \right) \quad (24)$$

where $k_{s\perp}$ and $k_{s\parallel}$ are the CRD wavenumber perpendicular and parallel to the line-of-sight direction.

Substituting equation (1), equation (24) reduces to

$$\begin{aligned} P^{(\text{CRD})}(k_{s\perp}, k_{s\parallel}; z) &= \frac{1}{c_\perp(z)^2 c_\parallel(z)} P^{(\text{R})} \left(\sqrt{\frac{k_{s\perp}^2}{c_\perp(z)^2} + \frac{k_{s\parallel}^2}{c_\parallel(z)^2}}; z \right) \\ &\times \left[\frac{k_{s\perp}^2}{c_\perp(z)^2} + \frac{k_{s\parallel}^2}{c_\parallel(z)^2} \right]^{-2} \left[\frac{k_{s\perp}^2}{c_\perp(z)^2} + \frac{\beta(z) + 1}{c_\parallel(z)^2} k_{s\parallel}^2 \right]^2 D \left[\frac{k_{s\parallel} \sigma_P(z)}{c_\parallel(z)} \right]. \end{aligned} \quad (25)$$

Introducing

$$k_s \equiv \sqrt{k_{s\perp}^2 + k_{s\parallel}^2}, \quad \mu_s \equiv k_{s\parallel}/k_s, \quad \eta \equiv c_\parallel/c_\perp, \quad (26)$$

the above result is rewritten as

$$\begin{aligned} P^{(\text{CRD})}(k_s, \mu_s; z) &= \frac{1}{c_\perp(z)^2 c_\parallel(z)} P^{(\text{R})} \left(\frac{k_s}{c_\perp(z)} \sqrt{1 + \left[\frac{1}{\eta(z)^2} - 1 \right] \mu_s^2}; z \right) \\ &\times \left[1 + \left(\frac{1}{\eta(z)^2} - 1 \right) \mu_s^2 \right]^{-2} \left[1 + \left(\frac{1 + \beta(z)}{\eta(z)^2} - 1 \right) \mu_s^2 \right]^2 \left[1 + \frac{k_s^2 \mu_s^2 \sigma_P^2}{2c_\parallel^2(z)} \right]^{-1}, \end{aligned} \quad (27)$$

where we adopt equation (11) for the damping function.

2.4. Comparison of the predicted anisotropy of the power spectrum with N-body simulations

In order to compute the power spectrum in CRD space, we employ the distant-observer approximation, calculate the power spectrum in comoving space, and finally transform it to that in the observed frame according to equation (24). We adopted this indirect procedure since we are mainly interested in the anisotropies in the power spectrum. As we will show in §3, however, even the angle-averaged power spectrum alone is useful as a cosmological test. Therefore in practice one would not have to take this route, but estimate the power spectrum directly in CRD space, because the distribution of objects obtained by observations has already been in the observed frame. We made sure that the estimate of the angle-averaged power spectrum from simulation data is almost identical even if we first transform the simulation volume into the CRD space and then compute the power spectrum.

In Figures 4a and 4b, we show the contours of power spectrum in CRD space at $z = 0$ and 2.2, respectively. In each figure, top panels correspond to theoretical predictions taking account of the linear velocity distortion alone but with the PD formulae for the power spectrum. Middle panels include the correction for the nonlinear finger-of-God using the MJB formulae in equation (27), and bottom panels plot the results from N-body simulations. As Cole et al.(1994) emphasized, the finger-of-God effect is appreciable even at $k_s \sim 0.2h\text{Mpc}^{-1}$ where the nonlinearity in *density field* is rather small.

In middle panels, solid and dotted contours refer to the the prediction using a Lorentzian and a Gaussian for the damping function, respectively. Despite the fact that the exponential does not perfectly match the distribution function of pairwise relative peculiar velocity derived from simulations, the agreement of theory and simulation in Figure 4 is rather well in this quasi-nonlinear regime. Nevertheless the direct analysis using the contour curves is still sensitive to the statistical noise in the data, and we instead are forced to use the multipole expansion as in our previous paper (Suto et al. 1999a):

$$P_l^{(\text{CRD})}(k_s; z) \equiv \frac{2l+1}{2} \int_{-1}^1 d\mu_s P^{(\text{CRD})}(k_s, \mu_s; z) L_l(\mu_s). \quad (28)$$

Figures 5 and 6 plot $P_0^{(\text{CRD})}(k_s)$ and $P_2^{(\text{CRD})}(k_s)$, the monopole and quadrupole moments of the power spectra, at $z = 0$ and 2.2. Filled and open circles represent the simulation results with all particles (1.7×10^7) and randomly selected particles (5×10^4), respectively. The quoted error bars refer to the dispersion among three different realizations in the case of all particles, and among 24 subsamples in total (i.e., 8 randomly selected subsamples for each realization) in the case of 5×10^4 particles. Note that the major difference in amplitude between the results with and without the geometrical effect in Figure 5 comes from the overall normalization factor $c_{\perp}(z)^2 c_{\parallel}(z)$ in equation (24). This is, however, a matter of definition to some extent, and what is important here is the difference among the cosmological models which is much smaller than the factor $c_{\perp}(z)^2 c_{\parallel}(z)$ (Ballinger et al. 1996; Matsubara & Suto 1996).

Numerical integration of equations (27) and (28) adopting the PD and MJB fitting formulae yields the corresponding theoretical predictions, which are plotted in thick solid and dotted lines for the exponential and Gaussian velocity distribution functions. Analytical results neglecting the cosmological distortion (eq.[12]) are shown in thin lines for reference. In any case the difference due to the modeling is negligible at $z = 0$, and the distortion at $z = 2.2$ is dominated by the geometrical effect.

Figures 5 and 6 indicate that the predictions based on the exponential velocity distribution function reproduce the simulation results fairly accurately, especially on large scales (small k_s). Also it is interesting and important to note that even the monopole component is significantly affected by the cosmological distortion. Figure 7 displays the predictions for the quadrupole to monopole ratio. In principle this statistics is superior either to the monopole or to the quadrupole in the sense that it is independent of the overall normalization of the power spectrum (e.g., Cole et al. 1995); in fact the ratio becomes constant, $(4\beta/3 + 4\beta^2/7)/(1 + 2\beta/3 + \beta^2/5)$, in linear regime (i.e., without finger of god and geometrical effects), which is plotted in dashed lines in the figure. On the other hand, the ratio lies between $-2 \sim 1$ and the practical usefulness crucially depends both on the data quality and the accuracy of the theoretical predictions (see §3 below).

In order to understand the model-dependence of the moments, we show the extent to which it is sensitive to the assumed velocity dispersions σ_P in Figure 8 for $P_0^{(\text{CRD})}(k_s)$, and to a set of parameters (Ω_0 , λ_0 , and Γ) in Figures 9, 10 and 11 for $P_0^{(\text{CRD})}(k_s)$, $P_2^{(\text{CRD})}(k_s)$, and $P_2^{(\text{CRD})}(k_s)/P_0^{(\text{CRD})}(k_s)$, respectively. Figure 8 implies that the predictions on scales $k_s \lesssim 0.2h\text{Mpc}^{-1}$ are very accurate and not sensitive to the adopted σ_P . Thus the usefulness of our proposed cosmological test is crucially dependent on the observational data quality on the quasi-linear scales which are presumably achievable only with the upcoming SDSS QSO surveys. It should be noted that there is a small but clear systematic difference between $N = 1.7 \times 10^7$ and 5×10^4 in Figures 5 to 8, despite the fact that we subtracted the shot noise due to the finite number of sampled particles. Actually we were not able to understand the origin of this effect, but the effect is smaller than the other uncertainties involved in the present analysis.

Incidentally Figure 9 indicates that the behavior of $P_0^{(\text{CRD})}(k_s)$ is degenerate for a certain set of the parameters since its shape and amplitude are sensitive both to Ω_0 and λ_0 through the correction factors, $c_\perp(z)$ and $c_\parallel(z)$, and to Γ through the shape of the power spectrum in real space. Such a degeneracy on the density parameter is apparent for open models of $\Gamma = 0.7\Omega_0$ and for flat models of $\Gamma = 0.2$. Fortunately, as shown by Figure 10, a measurement of the quadrupole $P_2^{(\text{CRD})}(k_s)$ may help break the degeneracy especially for the density parameter as low as ~ 0.2 . Combining other cosmological tests, such as the cosmic microwave background, clustering statistics, cluster abundances, etc. may further narrow the space of the cosmological parameters. In the next section we will investigate the feasibility of measuring the cosmological parameters by combining the first two moments of the red-shift power spectrum from a survey like the Sloan QSO survey and the cluster abundance.

3. Feasibility of determining the cosmological parameters from the power spectrum in cosmological redshift space

In the previous section we have demonstrated that the theoretical predictions for $P_0^{(\text{CRD})}(k_s; z)$ and $P_2^{(\text{CRD})}(k_s; z)$ are quite accurate for $k_s \lesssim 0.2h\text{Mpc}^{-1}$. Thus we finally examine if the cosmological test using these moments leads to any useful constraints on the cosmological parameters. For this purpose, we use the results from the N-body simulation models (Table 1) at $z = 2.2$, and perform the statistical analyses as follows.

Our theoretical model is specified by a set of Ω_0 , λ_0 , σ_8 , and h . Since the results of our N-body simulations are scalable with respect to h , we assume that h is related to the shape of the spectrum through the relation, $h \equiv \Gamma/\Omega_0$, neglecting the baryon contribution Ω_b (Sugiyama 1995) for simplicity. In order to take account of the statistical limitation, we do not use the entire simulation particles, but randomly select particles. For a given number of selected particles, we generate 24 mock samples (8 randomly selected subsamples for each realization) for each cosmological model. Then we assign the errors to the simulation data from the ensemble average over the 24 samples. In order to avoid the strongly nonlinear effect, we use the spectrum in the range $k_s \lesssim 0.2h\text{Mpc}^{-1}$, and perform the χ^2 -analysis.

Figures 12 and 13 display the confidence level contours from the χ^2 -analysis of $P_0^{(\text{CRD})}(k_s; z)$ or $P_2^{(\text{CRD})}(k_s; z)$ on Ω_0 - σ_8 and Ω_0 - λ_0 planes, respectively. To be specific, we compute the χ^2 defined by

$$\chi^2 = \sum_{i=1}^{10} \left[\frac{P_{\text{sim}}^{R,S}(k_{s,i}) - P_{\text{model}}(k_{s,i})}{\Delta_{\text{Psim}}(k_{s,i})} \right]^2, \quad (29)$$

where the wavenumber is sampled between $0.02h\text{Mpc}^{-1} \lesssim k_s \lesssim 0.2h\text{Mpc}^{-1}$ as

$$k_{s,i} = \frac{2\pi}{L_{\text{box}}} i \quad (i = 1, \dots, 10). \quad (30)$$

The indices R and S denote the three different realizations and eight randomly selected subsamples for each cosmological model, and in evaluating equation (29) we randomly choose one mock sample from 24 ($= 3 \times 8$) simulated mock samples in total. For $\Delta_{\text{Psim}}^2(k_{s,i})$, we use the dispersion among 24 mock samples assuming that this corresponds to a cosmic variance:

$$\bar{P}_{\text{sim}}(k_{s,i}) = \frac{1}{24} \sum_{R=1}^3 \sum_{S=1}^8 P_{\text{sim}}^{R,S}(k_{s,i}) \quad (31)$$

$$\Delta_{\text{Psim}}^2(k_{s,i}) = \frac{1}{24-1} \sum_{R=1}^3 \sum_{S=1}^8 [P_{\text{sim}}^{R,S}(k_{s,i}) - \bar{P}_{\text{sim}}(k_{s,i})]^2. \quad (32)$$

The resulting confidence level is computed from the reduced χ^2 for eight degrees of freedom, i.e., ten data points *minus* two free parameters, either, (Ω_0, σ_8) or (Ω_0, λ_0) . We perform the above analysis for the monopole and the quadrupole, separately, and also combine the monopole and quadrupole

analysis. We have adopted the χ^2 technique to quantify the errors for the measured parameters because it is simple, but perhaps other statistical methods, e.g., the maximum likelihood, may better quantify the measurement errors in the actual application to the future observational data.

Figures 12a, 12c, 13a, and 13c assume that $\Gamma = \Omega_0 h$, while other panels in these two figures treat Γ as an independent parameter and fix the value as specified by the simulation (Table 1). We display the results for $N = 5 \times 10^5$ (bottom panels), 5×10^4 (middle panels), and 5×10^3 (top panels) from the entire 256^3 particles at $z = 2.2$. For reference, the quasar luminosity function of Boyle, Shanks, & Peterson (1988) predicts that the number of quasars per π steradian brighter than 19 magnitude in B is about 4500 either in $z = 0.9 \sim 1.1$ or in $z = 1.9 \sim 2.1$ (for the $\Omega_0 = 1$ and $\lambda_0 = 0$ model). If we use the extrapolation of the luminosity function to $z \sim 5$ by Wallington & Narayan (1993), the total number of $\sim 10^5$ QSOs $0 \lesssim z \lesssim 5$ are expected to be cataloged in the upcoming SDSS QSO sample. It should be noted that the best-fit parameters in those figures are sometimes a bit different from the true values that we use in the simulations. This is simply because the figures represent results for one particular mock sample. We made sure that the best-fit values are in good agreement with the true values if we replace $P_{\text{sim}}^{R,S}(k_{s,i})$ in equation (29) by $\bar{P}_{\text{sim}}(k_{s,i})$.

We repeat the analysis in Figure 12 by fixing either $\lambda_0 = 0$ or $= 1 - \Omega_0$. As anticipated, the present analyses with either $P_0^{(\text{CRD})}(k_s)$ or $P_2^{(\text{CRD})}(k_s)$ alone do not determine the cosmological parameters completely. However, the error contours of the monopole do not align with those of the quadrupole completely; in some cases the contours of the monopole and the quadrupole are somewhat orthogonal, though the error contours of the quadrupole are generally larger than those of the monopole. These results indicate that a combination of the first two moments can more stringently, as expected, constrain the cosmological parameters. Figures 14 show the confidence levels of such a joint constraint on (σ_8, Ω_0) . An encouraging feature noted from this figure is that the flat and open universes with $\Omega_0 = 0.3$ can be well separated with this test if the number of the objects $N \geq 5 \times 10^4$. Nevertheless the combination with another cosmological test can easily yield an interesting constraint in the parameter space. This is illustrated in the middle panels of Figures 12 and 14 where the constraints from the X-ray cluster abundance (Kitayama & Suto 1997):

$$\sigma_8 = (A \pm 0.02) \times \begin{cases} \Omega_0^{-0.35-0.82\Omega_0+0.55\Omega_0^2} & (\lambda_0 = 1 - \Omega_0), \\ \Omega_0^{-0.28-0.91\Omega_0+0.68\Omega_0^2} & (\lambda_0 = 0). \end{cases} \quad (33)$$

are overlaid. The normalization factor A determined from the observed cluster abundance is 0.54.

Combining the cluster abundance with the test of this paper may determine the cosmological parameters λ_0 and Ω_0 . This is illustrated in Figure 13. The normalization σ_8 adopted in our simulations are slightly different from the value given by Eq.(33). Thus in the analysis presented in Figures 13 and 15, we accordingly change the normalization factor A with keeping the same Ω_0 dependence, and find the minimal χ^2 by allowing the ± 0.02 dispersion. Our adopted value of A for each model is summarized in Table 1. The monopole moment is sensitive to the density parameter Ω_0 only, while the quadrupole measurement interestingly complements to the monopole measurement in that it depends more strongly on the cosmological constant. Combining these

two moments results in a joint constraint on (Ω_0, λ_0) which is shown in 15. Consistent with the results shown in Figure 14, the open and flat universes with $\Omega_0 \lesssim 0.3$ can be discriminated with the number of objects larger than 5×10^4 . It is also interesting to note that our constraints in Figure 15 are fairly orthogonal to those from the SN Ia (Perlmutter et al. 1999), and can be even combined to probe the cosmic equation of state in general (e.g., Garnavich et al. 1998).

Finally we repeat the similar analysis for the quadrupole to monopole ratio, the results of which are plotted in Figure 16. As anticipated the resulting constraints are more sensitive to λ_0 compared to those presented in Figures 15. On the other hand, we realize that our current modeling may not be sufficiently good to describe the ratio in practice; note that while the amplitudes of the monopole and the quadrupole span two orders of magnitudes, their ratio is merely around between -2 and 1 , and thus the accurate modeling and good data qualities are required for the robust estimation of the cosmological parameters. This is why some panels in Figure 16 do not have any contours with reasonable confidence levels.

4. Conclusions and discussion

In this paper, we have examined the reliability and accuracy of the theoretical modeling for the power spectrum in cosmological redshift space using the high-resolution N-body simulations. Our main conclusion is that the cosmological test proposed by Ballinger et al. (1996) and Matsubara & Suto (1996) is in fact practically useful in constraining the cosmological parameters combined with the upcoming SDSS QSO sample. While an application of this methodology to the Lyman-break galaxies is also interesting, the small number of total objects and cosmic variance seem to be the major difficulties in practice (Nair 1999). The results are admittedly complicated since many different and important contaminations are necessarily involved. In particular, our methodology is heavily dependent on the underlying mass power spectrum, which may be reconstructed from the redshift-space observation but with large uncertainties. Thus we explicitly assume that the spectrum is completely specified by four free parameters, Ω_0 , λ_0 , Γ and σ_8 , as in the case of CDM models. More importantly and realistically, any model for bias should add at least another free parameter (even in a time-independent and scale-invariant linear model which is too idealistic). As a result, the estimated parameters are inevitably model-dependent. Therefore in order to extract useful cosmological information, we have to combine the additional constraints on those parameters from independent cosmological consideration. Even so, the present model is a minimal requirement to understand the clustering of high-redshift objects properly.

The remaining important problems to improve this cosmological test include the higher-order moment analysis, the biasing and the light-cone effects; first, we have shown that the anisotropy of the power spectrum in cosmological redshift space shows up already in the monopole and quadrupole moments, $P_0^{(\text{CRD})}(k_s)$ and $P_2^{(\text{CRD})}(k_s)$. On the other hand, this is why the resulting constraints are only weakly dependent on λ_0 , unlike the original idea by Alcock & Paczyński (1979); note, however, that Ballinger et al. (1996) correctly recognized this difficulty. Utilizing the higher-order

moments will be another possibility, although the data will be necessarily noisier. Second, our analysis presented above implicitly assumes to apply for the data in a narrow redshift bin. In order to increase the number of available pairs, and thus the statistical significance, it is crucial to take account of the cosmological light-cone effect properly in theoretical predictions following Yamamoto & Suto (1999), Yamamoto, Nishioka, & Suto (1999) and Suto et al. (1999a). Finally, we did not allow for the possible biasing which should further complicate the mapping of the clustering statistics of the luminous objects to that of the underlying mass distribution. These issues will be discussed elsewhere (Magira, Jing, Taruya, & Suto 1999).

We thank Takahiko Matsubara for discussion, and the referee, Alan Heavens, for several constructive comments. Y. P. J. gratefully acknowledges support from a JSPS (Japan Society for the Promotion of Science) fellowship. Numerical computations presented were carried out on VPP300/16R and VX/4R at ADAC (the Astronomical Data Analysis Center) of the National Astronomical Observatory, Japan, as well as at RESCEU (Research Center for the Early Universe, University of Tokyo) and KEK (High Energy Accelerator Research Organization, Japan). This research was supported in part by the Grant-in-Aid by the Ministry of Education, Science, Sports and Culture of Japan (07CE2002) to RESCEU, and by the Supercomputer Project (No.98-35 and No.99-52) of KEK.

REFERENCES

- Alcock, C., & Paczyński, B. 1979, *Nature*, 281, 358
- Ballinger, W. E., Peacock, J. A., & Heavens, A. F. 1996, *MNRAS*, 282, 877
- Bardeen, J. M., Bond, J. R., Kaiser, N., & Szalay, A. S. 1985, *ApJ*, 304, 15
- Boyle, B. J., Shanks, T., & Peterson, B. A. 1988, *MNRAS*, 235, 935
- Cole, S., Fisher, K. B., & Weinberg, D. H. 1994, *MNRAS*, 267, 785
- Cole, S., Fisher, K. B., & Weinberg, D. H. 1995, *MNRAS*, 275, 515
- Davis, M., & Peebles, P. J. E. 1983, *ApJ*, 267, 465
- Dekel, A. , & Lahav, O. 1999, *ApJ*, 520, 24
- de Laix, A. A., & Starkman, G. D. 1998, *MNRAS*, 299, 977
- Efstathiou, G., Frenk, C. S., White, S. D. M., & Davis, M. 1988, *MNRAS*, 235, 715
- Fan, X., et al. 1999, *AJ*, 117, in press (astro-ph/9903237)
- Fry, J. N. 1996, *ApJ*, 461, L65
- Garnavich, P. M., et al. 1998, *ApJ*, 509, 74
- Haiman, Z., & Loeb, A. 1999, *ApJ*, 521, L9
- Hamilton, A. J. S. 1998, in “ The Evolving Universe. Selected Topics on Large-Scale Structure and on the Properties of Galaxies”, (Kluwer: Dordrecht), p.185
- Hatton, S., & Cole, S. 1998, *MNRAS*, 296, 10
- Jing, Y. P. 1992, ph.D.thesis, SISSA, Trieste
- Jing, Y. P. 1998, *ApJ*, 503, L9
- Jing, Y. P., & Suto, Y. 1998, *ApJ*, 494, L5
- Juszkiewicz, R., Fisher, K. B., & Szapudi, I. 1998, *ApJ*, 504, 1
- Kaiser, N. 1984, *ApJ*, 284, L9
- Kaiser, N. 1987, *MNRAS*, 227, 1
- Kitayama, T., & Suto, Y. 1997, *ApJ*, 490, 557
- La Franca, F., Andreani, P., & Cristiani, S. 1998, *ApJ*, 497, 529
- Lahav, O., Piran, T., & Treyer, M. 1997, *MNRAS*, 284, 499
- Magira, H., Jing, Y. P., Taruya, & Suto, Y. 1999, in preparation
- Matarrese, S., Coles, P., Lucchin, F., & Moscardini, L. 1997, *MNRAS*, 286, 115
- Matsubara, T., & Suto, Y. 1996, *ApJ*, 470, L1
- Matsubara, T., Suto, Y., & Szapudi, I. 1997, *ApJ*, 491, L1
- Mo, H. J., & White, S. D. M. 1996, *MNRAS*, 282, 347
- Mo, H. J., Jing, Y. P., & Börner, G. 1997, *MNRAS*, 286, 979 (MJB)
- Moscardini, L., Coles, P., Lucchin, F., & Matarrese, S. 1998, *MNRAS*, 299, 95
- Nakamura, T. T., Matsubara, T., & Suto, Y. 1998, *ApJ*, 494, 13
- Nair, V. 1999, *ApJ*, in press (astro-ph/9904312)
- Nishioka, H., & Yamamoto, K. 1999, *ApJ*, 520, 426
- Peacock, J. A., & Dodds, S. J. 1994, *MNRAS*, 267, 1020
- Peacock, J. A., & Dodds, S. J. 1996, *MNRAS*, 280, L19 (PD)
- Perlmutter, S., et al. 1999, *ApJ*, 517, 565
- Popowski, P. A., Weinberg, D. H., Ryden, B. S., & Osmer, P. S. 1998, *ApJ*, 498, 11
- Seto, N., & Yokoyama, J. 1998, *ApJ*, 492, 421
- Steidel, C. C., Giavalisco, M., Pettini, M., Dickinson, M., & Adelberger, K. L. 1996, *ApJ*,

- 462, L17
- Steidel, C. C., Adelberger, K. L., Dickinson, M., Giavalisco, M., Pettini, M., & Kellogg, M. 1998, *ApJ*, 492, 428
- Sugiyama N. 1995, *ApJS*, 100, 281
- Suto, Y. 1993, *Prog.Theor.Phys.*, 90, 1173
- Suto, Y., Magira, H., Jing, Y. P., Matsubara, T., & Yamamoto, K. 1999a, *Prog.Theor.Phys.Suppl.*, 133, 183
- Suto, Y., Yamamoto, K., Kitayama, T., & Jing, Y. P. 1999b, *ApJ*, submitted (astro-ph/9907105)
- Suto, Y., & Sugihara, T. 1991, *ApJ*, 370, L15
- Taruya, A., Koyama, K., & Soda, J. 1999, *ApJ*, 510, 541
- Treyer, M., Scharf, C., Lahav, O., Keith, J., Boldt, E., & Piran, T. 1998, *ApJ*, 509, 531
- Ueda, H., Itoh, M., & Suto, Y. 1993, *ApJ*, 408, 3
- Wallington, S., & Narayan, R. 1993, *ApJ*, 403, 517
- Yamamoto, K., & Suto, Y. 1999, *ApJ*, 517, 1
- Yamamoto, K., Nishioka, H., & Suto, Y. 1999, *ApJ*, in press

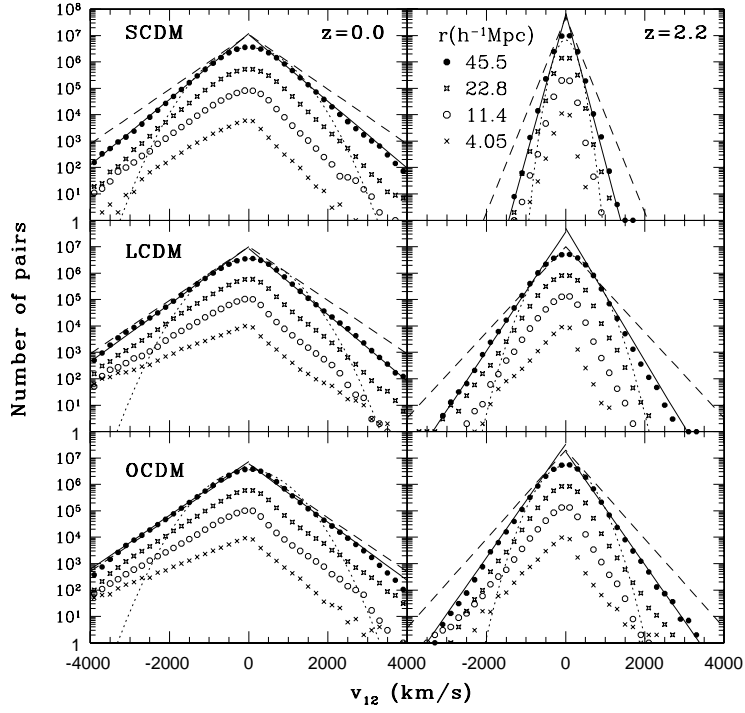


Fig. 1.— Pairwise peculiar velocity distribution for different cosmological models at $z = 0$ and $z = 2.2$. We compute the number of particles plotted is within a velocity bin of $\Delta v_{12} = 200\text{km/s}$. Different symbols indicate the results from N-body simulations at different pair-separation; $r = 46$ (filled circles), 23 (stars), 11 (open circles) and $4.1 h^{-1}\text{Mpc}$ (crosses). Solid lines in each panel represent the best fit to the exponential distribution function (eq.[7]) treating σ_P as a free parameter. Dashed and dotted lines display the exponential and Gaussian functions, respectively, with $\sigma_P = \sigma_{P,\text{sim}}$.

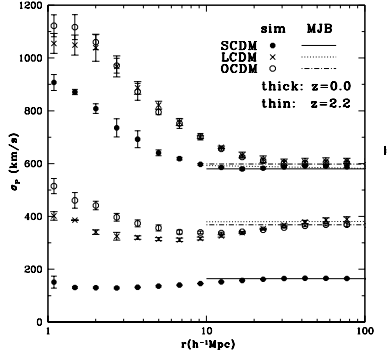


Fig. 2.— Pairwise peculiar velocity dispersions for different cosmological models. Thick and thin lines correspond to the prediction (9) at $z = 0$ and $z = 2.2$, respectively. Different symbols correspond to the results of N-body simulations. Error bars represent the standard deviation among three realizations for each model.

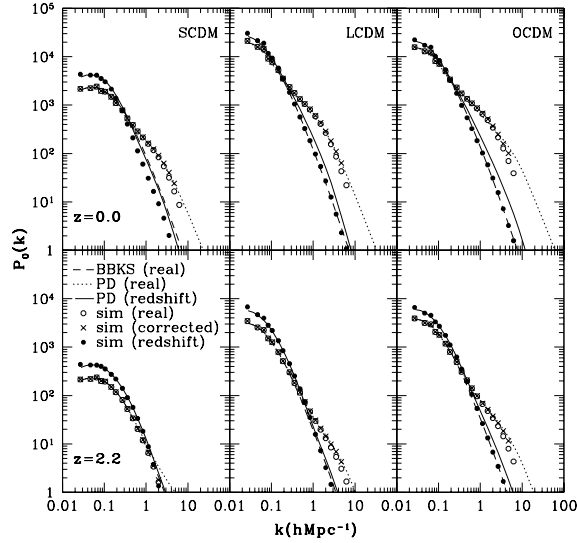


Fig. 3.— The monopole of power spectra at $z = 0$ (upper panels) and $z = 2.2$ (lower panels) neglecting the geometrical effect in the redshift-space distortion. Dashed and dotted curves correspond to theoretical prediction based on the BBKS and PD formulae for power spectrum in real space, respectively. Solid curves show the predictions in redshift space combining the PD formula and the Lorentzian damping function. Different symbols indicate the results of our N-body simulations in real (open circles) and redshift (filled circles) space. The crosses refer to the power spectrum in real space which is corrected for the smoothing effect in the FFT.

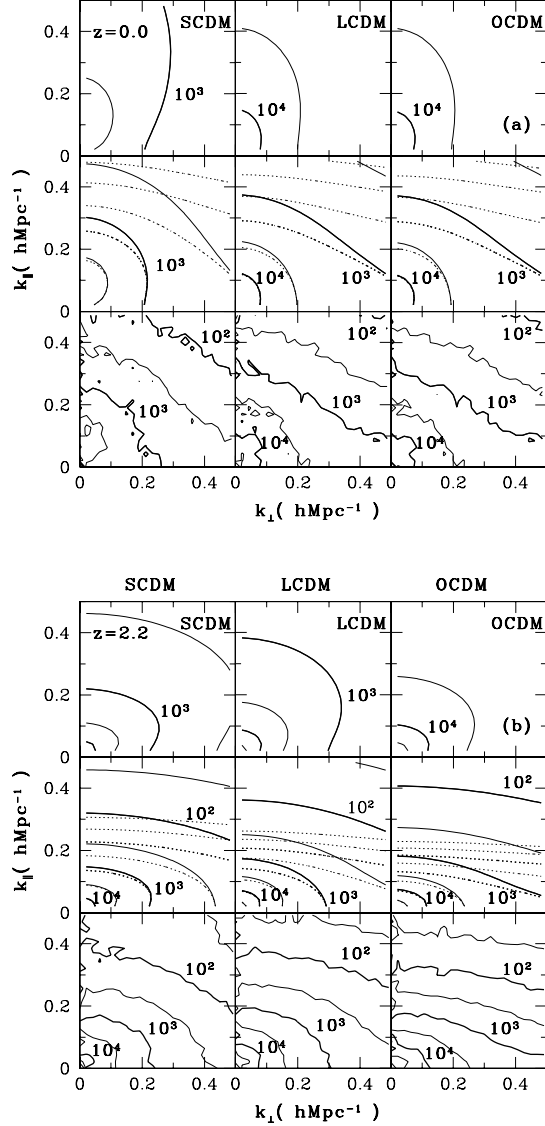


Fig. 4.— Two-dimensional power spectra in cosmological redshift space; (a) $z = 0$, (b) $z = 2.2$. In each figure, the upper panels display the predictions with the PD mass power spectrum and linear velocity distortion. The middle panels display the predictions with the PD mass power spectrum and non-linear velocity distortion. The Lorentzian (solid) and Gaussian (dotted) are adopted for the damping function describing the nonlinear velocity distortion (with $\sigma_P = \sigma_{P,MJB}$). The bottom panels display the power spectrum calculated from N-body simulations with all the particles ($N = 256^3$).

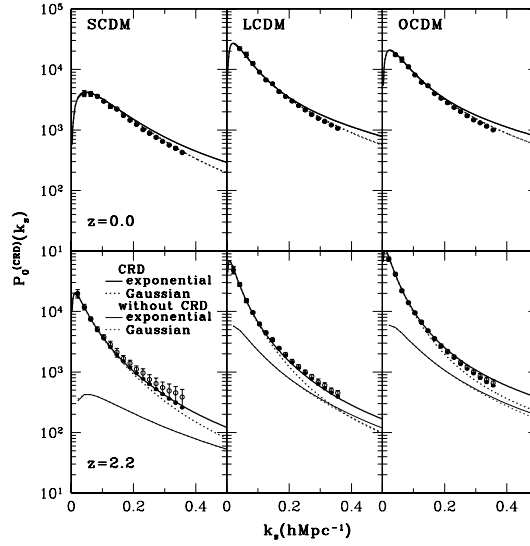


Fig. 5.— The monopole of power spectra for different cosmologies at $z = 0$ (upper panels) and $z = 2.2$ (lower panels). Filled and open circles correspond to the results from N-body simulation, which are evaluated from all particles (1.7×10^7) and selected particles (5×10^4), respectively. Thick curves correspond to the predictions including cosmological redshift distortion effect with an exponential (solid) and Gaussian (dotted) damping function, respectively. For reference, the predictions neglecting the geometrical effect at $z = 2.2$ are shown in thin curves (eq.[12]).

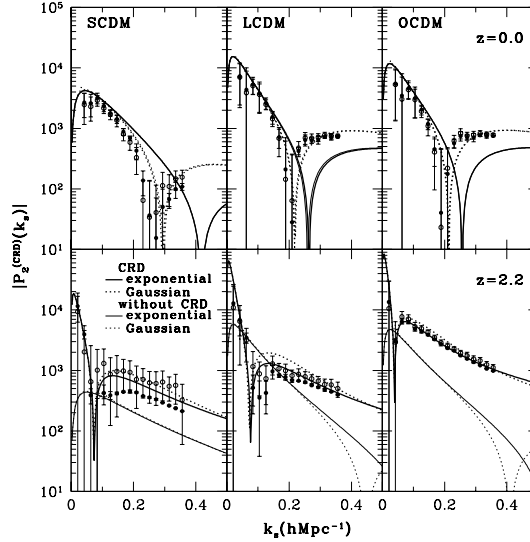


Fig. 6.— The same as Figure 5 but for the quadrupole moment of the power spectra.

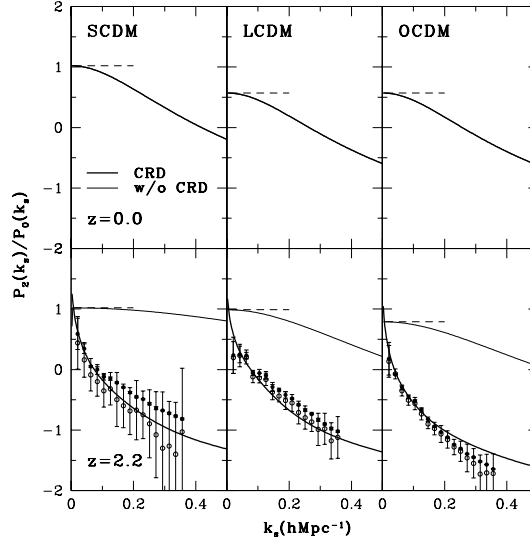


Fig. 7.— The same as Figure 5 but for the quadrupole to monopole ratio.

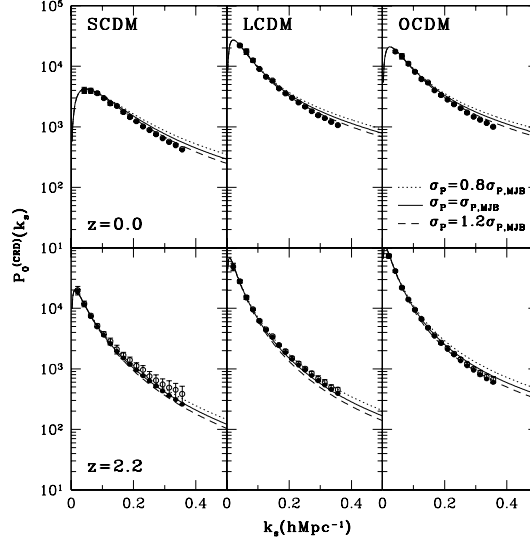


Fig. 8.— Dependence of the monopole of power spectra on the velocity dispersions at $z = 0$ (upper panels) and $z = 2.2$ (lower panels) in CRD space; σ_p is set to be $0.8\sigma_{p,MJB}$ (dotted lines), $\sigma_{p,MJB}$ (solid lines), and $1.2\sigma_{p,MJB}$ (dashed lines). Filled and open circles correspond to the results from N-body simulation, which are evaluated from all particles (1.7×10^7) and selected particles (5×10^4), respectively.

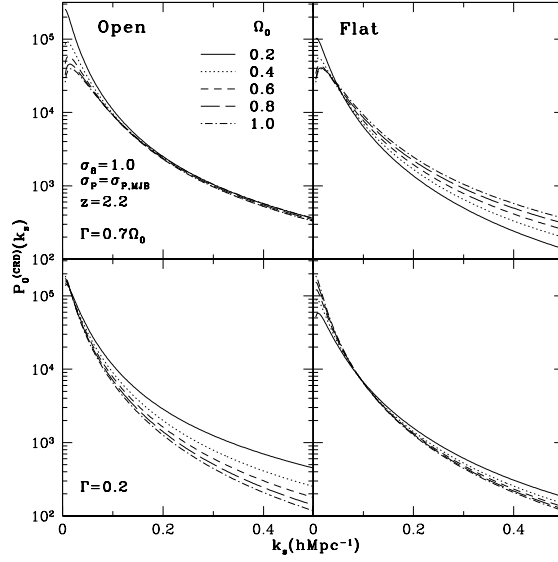


Fig. 9.— Dependence of the monopole of power spectra in cosmological redshift space at $z = 2.2$ on Ω_0 . We consider both open ($\lambda_0 = 0$) and spatially-flat ($\lambda_0 = 1 - \Omega_0$) models in left and right panels, respectively. The shape parameter Γ is fixed as $0.7\Omega_0$ in upper, and 0.2 in lower panels. The fluctuation amplitude σ_8 is fixed as unity for simplicity.

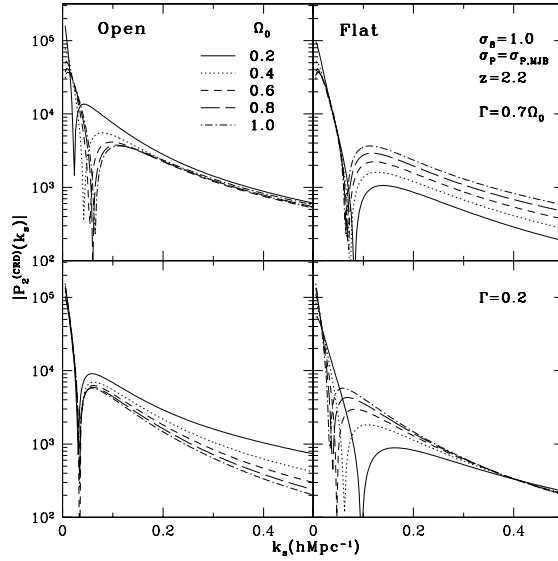


Fig. 10.— The same as Figure 9 but for the quadrupole moment of the power spectra.

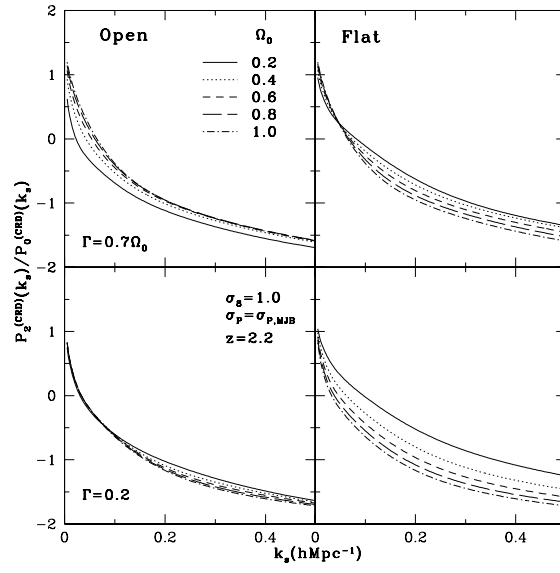


Fig. 11.— The same as Figure 9 but for the quadrupole to monopole ratio.

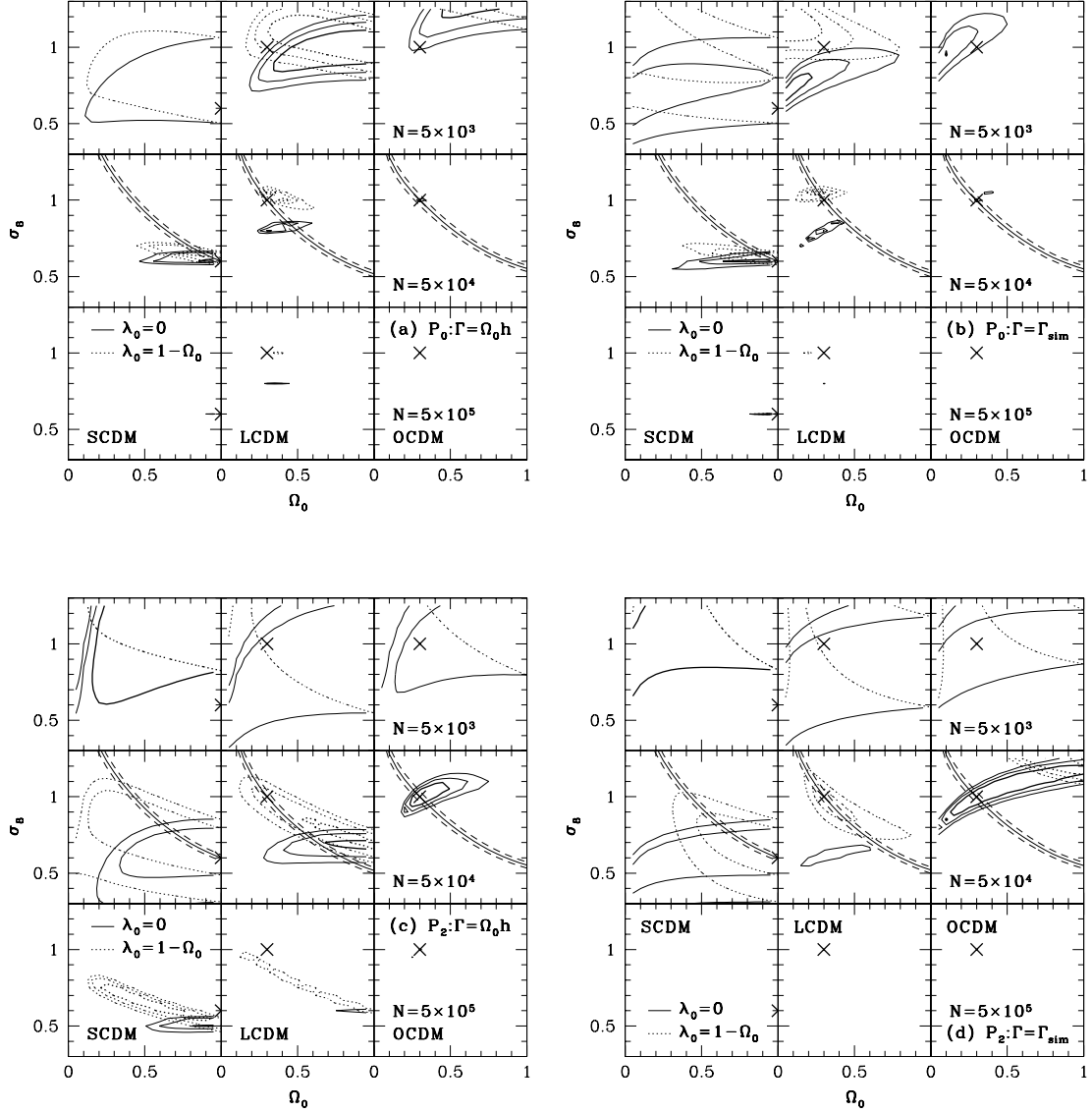


Fig. 12.— The confidence contours on Ω_0 - σ_8 plane from the χ^2 -analysis of the monopole and quadrupole moments of the power spectrum in the cosmological redshift space at $z = 2.2$; (a) $\Gamma = \Omega_0 h$ for $P_0^{(\text{CRD})}(k_s)$, (b) $\Gamma = \Gamma_{sim}$ for $P_0^{(\text{CRD})}(k_s)$, (c) $\Gamma = \Omega_0 h$ for $P_2^{(\text{CRD})}(k_s)$, (d) $\Gamma = \Gamma_{sim}$ for $P_2^{(\text{CRD})}(k_s)$. The long-dashed, heavy thick, light thick, and thin lines correspond to 0.5, 1, 2, and 3σ confidence levels. We randomly selected $N = 5 \times 10^3$ (upper panels), $N = 5 \times 10^4$ (middle panels), and $N = 5 \times 10^5$ (lower panels) particles from N-body simulation. Solid and dotted lines represent results for open and spatially-flat models, respectively. The crosses indicate the true values of our simulations. We also show the constraint on Ω_0 and σ_8 from the cluster abundance by thin lines in the middle panels.

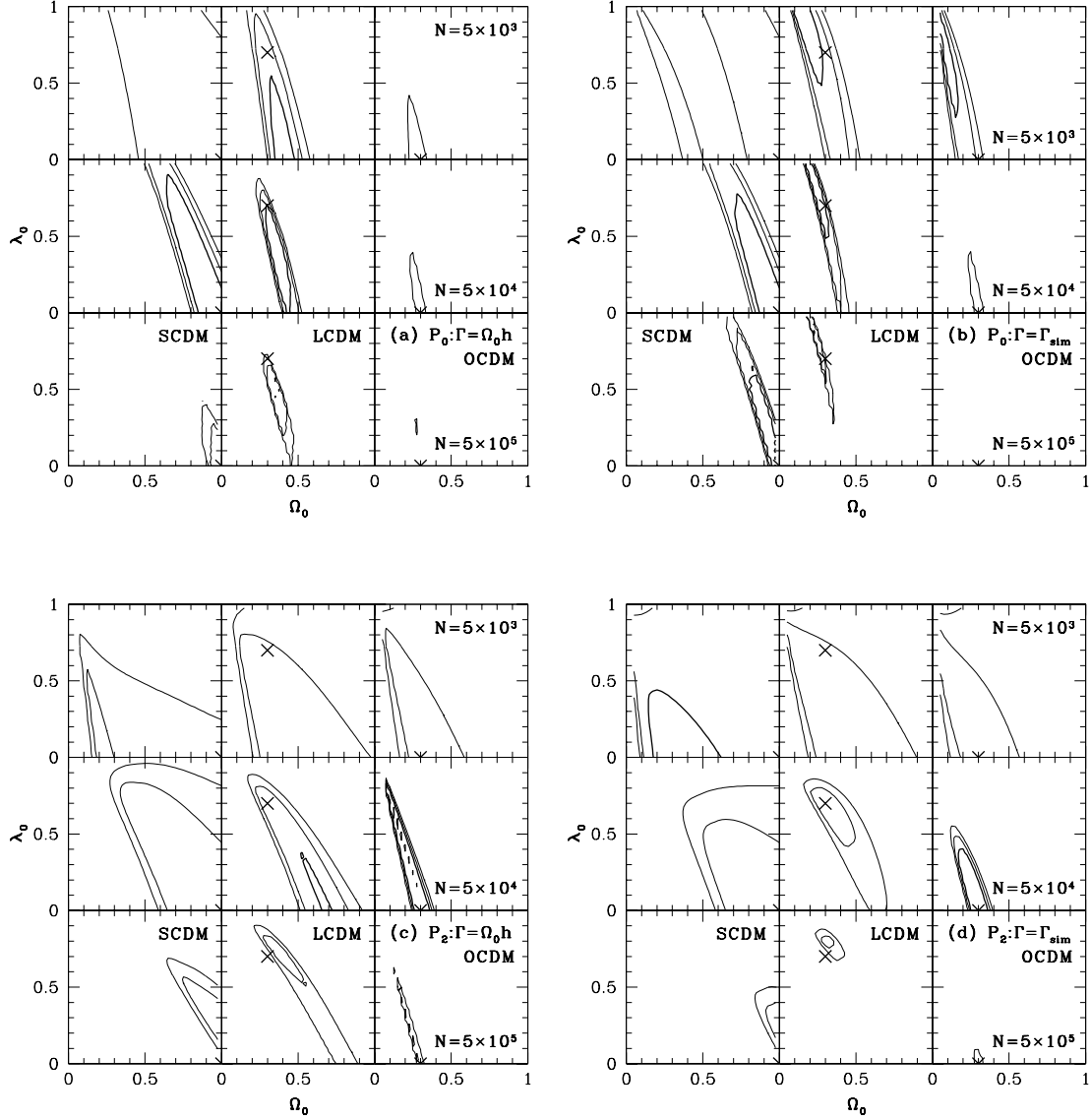


Fig. 13.— The same as Figure 12 but on Ω_0 - λ_0 plane. We adopt the value of σ_8 from equation (33) with the quoted error bars.

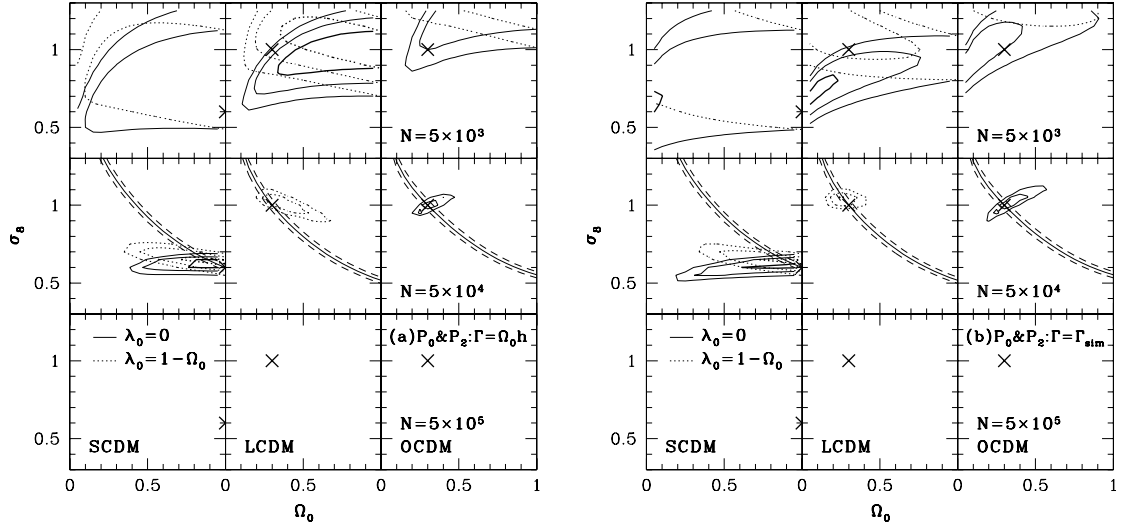


Fig. 14.— The same as Figure 12 but from the combined analysis of the monopole and quadrupole moments.

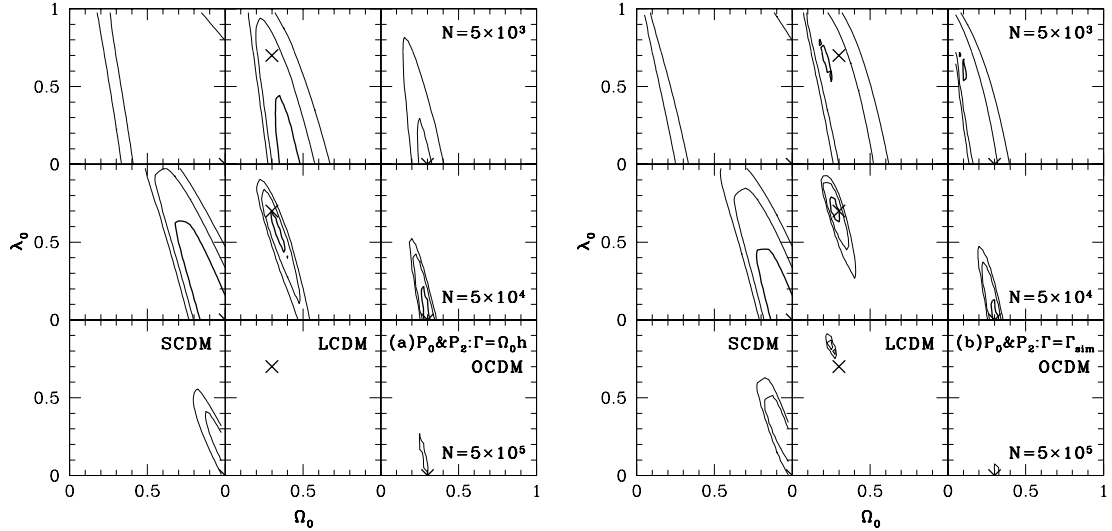


Fig. 15.— The same as Figure 13 but from the combined analysis of the monopole and quadrupole moments.

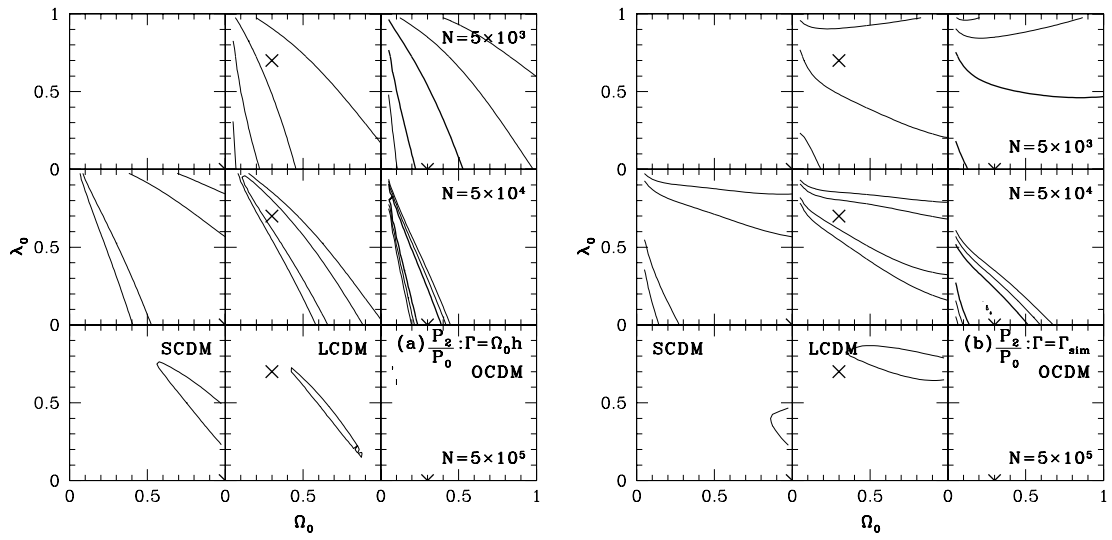


Fig. 16.— The same as Figure 13 but from the analysis of the quadrupole to monopole ratio.

Table 1: Simulation model parameters.

| Model | Ω_0 | λ_0 | Γ^a | σ_8 | N | h^b | A^c | realizations |
|---------------------|------------|-------------|------------|------------|---------|-------|-------|--------------|
| SCDM (Standard CDM) | 1.0 | 0.0 | 0.5 | 0.6 | 256^3 | 0.50 | 0.60 | 3 |
| LCDM (Lambda CDM) | 0.3 | 0.7 | 0.21 | 1.0 | 256^3 | 0.70 | 0.52 | 3 |
| OCDM (Open CDM) | 0.3 | 0.0 | 0.25 | 1.0 | 256^3 | 0.83 | 0.55 | 3 |

^athe shape parameter of the power spectrum.

^bthe dimensionless Hubble constant *defined* through $h \equiv \Gamma/\Omega_0$ neglecting the baryon density parameter $\Omega_b = 0$.

^cthe normalization factor of σ_8 - Ω_0 relation determined from the X-ray cluster abundance (Kitayama & Suto 1997).

Table 2: Pairwise peculiar velocity dispersions at $z = 0$ and 2.2.

| Model | z | $\sigma_{P,MJB}$ [km/s] | $\sigma_{P,sim}$ [km/s] ^a | $\sigma_{P,fit}$ [km/s] ^b | fitting range[km/s] ^c |
|-------|-----|-------------------------|--------------------------------------|--------------------------------------|----------------------------------|
| SCDM | 0 | 580 | 592 | 493 | 900 - 2900 |
| LCDM | 0 | 582 | 606 | 563 | 900 - 2900 |
| OCDM | 0 | 599 | 603 | 602 | 900 - 2900 |
| SCDM | 2.2 | 164 | 166 | 113 | 100 - 1100 |
| LCDM | 2.2 | 381 | 379 | 273 | 900 - 2900 |
| OCDM | 2.2 | 368 | 365 | 287 | 900 - 2900 |

^aa relative pairwise peculiar velocity dispersion directly evaluated from the N-body data at $r = 42h^{-1}$ Mpc.

^ba relative pairwise peculiar velocity dispersion evaluated through a fit to the exponential distribution function.

^ca range of v_{12} for the fit.